Sustainable Energy & Fuels

PAPER

View Article Online
View Journal | View Issue

Cite this: *Sustainable Energy Fuels*, 2020, **4**, 380

Tuning the surface segregation composition of a PdCo alloy by the atmosphere for increasing electrocatalytic activity†

Tongtong Li,‡[a] Rong Wang,‡[b] Minghe Yang,[a] Shuaishuai Zhao,[a] Zhijie Li,[a] Junjian Miao,[b] Zhi-Da Gao,[a] Yi Gao *[bc] and Yan-Yan Song *[a]

Received 7th August 2019
Accepted 16th October 2019

DOI: 10.1039/c9se00620f

rsc.li/sustainable-energy

The rational design of active sites for electrocatalysts is crucial for achieving high efficiency of electrochemical reactions. Contrary to the shape-controlled method, herein, we reported a selective segregation-etching strategy to highly increase the active sites of a bimetallic alloy as a high-performance electrocatalyst. The surface composition of the PdCo alloy was manipulated by its preferential segregation in the atmosphere according to the predictions of the density functional theory (DFT). By leaching Co atoms from the surface having a balanced composition with consecutive potential cycling in an acid solution, the surface reconstructed to show a high density of high-index Pd facets identified by Cs-corrected transmission electron microscopy. Using hydrogen evolution as a model reaction, the resulting catalyst exhibited enhanced electrocatalytic activity and outstanding long-term stability. This study provides a general principle to design a transition metal alloy with highly active sites, which has a great potential in broad areas such as batteries, fuel cells, and beyond.

1. Introduction

The performance of nanocatalysts is determined by their composition and active sites.[1–3] Correspondingly, two strategies have been widely employed in the past decades. One involves adding cheap impurities into noble metal nanocrystals to reduce the cost and tune the electronic structures.[4,5] Another involves the use of shape-controlled methods to present more active sites.[6–10] Generally, low-coordinated sites have higher catalytic activities.[11] To increase the active sites, it is necessary to increase the number of low-coordinated sites and decrease their coordination number. Shape-controlled synthesis involves the use of different adsorption capacities between ligands and surfaces to increase the ratio of high-index facets.[12,13] However, the delicate control of the shape of nanocrystals with high-index facets is always challenging. Some electrochemical methods such as square wave potential and fast potential cycles have been applied to successfully synthesize tetrahexahedral (THH) Pt nanocubes with a high-index plane from nanospheres.[14] Here, we presented a selective segregation-etching strategy to synthesize nanocrystals with high density of active sites without tuning shapes. Using a PdCo alloy as the model system, the synthesized nanocatalyst exhibited significant activity and stability toward the hydrogen evolution reaction (HER).

Hydrogen, a renewable energy source, provides a promising solution for the growing concerns about global warming and diminishing fossil fuels.[15–17] One of the efficient and renewable approaches for producing hydrogen is electrochemical water splitting.[18,19] Palladium (Pd), which resembles Pt in many respects, is one of the most competitive candidates as Pt's replacements due to its widespread resource in the Earth's crust and excellent catalytic abilities for various oxidation and reduction electrode processes.[20,21] Contrary to previous strategies, such as preparing specific Pd facets, controlling composition and morphology,[22,23] finding advanced substrates,[24] and creating Pd alloys,[25] our idea involved the use of the varied segregation preferences of the Pd alloy in different conditions to generate facets with a balanced composition. Then, when we etched the impurity points out of these surfaces, the abundant vacancies on the surface generated the maximum number of neighbouring Pd atoms as low-coordinated sites, that is, the active sites. This selective segregation-etching strategy is shown in Scheme 1.

To fulfill this strategy, we first used a cyanogel as the bimetal precursor to create a PdCo alloy.[26,27] Then, based on the density functional theory calculations, we applied a suitable

[a]College of Sciences, Northeastern University, Shenyang 110004, China. E-mail: yysong@mail.neu.edu.cn

[b]Shanghai Institute of Applied Physics, Chinese Academy of Sciences, Shanghai 201800, China. E-mail: gaoyi@sinap.ac.cn

[c]Shanghai Advanced Research Institute, Chinese Academy of Sciences, Shanghai 201800, China

† Electronic supplementary information (ESI) available: Additional structural and compositional characterizations, adsorption configurations and their corresponding adsorption energies of different atmosphere on different metal surfaces, TOF calculations and comparison of HER performance. See DOI: 10.1039/c9se00620f

‡ These authors contributed equally to this work.

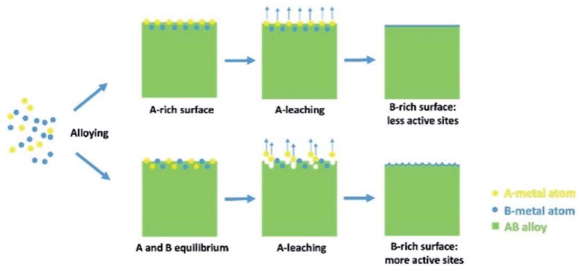

Scheme 1 Schematic illustration of the selective segregation-etching strategy to generate alloy surface with more low-coordinated sites.

atmosphere to tune the surface segregation preference. Furthermore, the segregated PdCo alloy with the balanced composition on the surfaces was controllably etched by electrochemical (EC) cycling in an acid solution to leach Co surface atoms. This selective segregation-etching strategy afforded high density of high-index Pd crystallographic facets on the rearranged surface to achieve a significant elevation of the HER activity of the catalyst, which provided a general principle to design metal nanocatalysts with high active sites.

2. Results and discussion

2.1 Design of surface composition of PdCo by the atmosphere

A cyanogel was used in this experiment to synthesize a PdCo alloy. The initially synthesized nanoparticles were protected by cyanide (CN) ligands.[26] It is known that the surface composition of alloys is highly influenced by the adsorbed molecules due to their different affinities to different metal elements. In this case, to tune the surface composition of the PdCo alloy, we carried out density functional theory (DFT) calculations to compare the binding energies of cyanide (CN), Ar and NH_3 with the Pd/Co surfaces, as shown in Table 1. Three low-index surfaces (111), (100), and (110) were calculated. All the adsorption configurations can be found in Table S1–S3.† The adsorption of CN on all the Co and Pd surfaces was very strong (>3 eV) and the adsorption affinities of CN on the Co surfaces were substantially higher than those on Pd. The adsorption energies of NH_3 on the Pd and Co surfaces were very close and moderately strong (~0.8 eV). On the contrary, the binding energies of Ar on all the Co and Pd surfaces were close to zero. Based on the above calculations, we could reasonably conclude that CN greatly increased the Co/Pd equilibrium ratio even in a low concentration, while the NH_3 adsorption may induce a balanced Co/Pd ratio. Ar exhibited negligible effects on the PdCo composition, which was consistent with previous results.[28] Thus, if we want to tune the PdCo alloy from a Co-rich surface to a PdCo-balanced surface, replacing CN with NH_3 can be a viable pathway, as shown in Fig. 1.

Table 1 Calculated binding energies of CN, NH_3 and Ar on Pd and fcc-Co pure surfaces (in eV)

	CN		NH_3		Ar	
Facet	Pd	Co	Pd	Co	Pd	Co
(100)	−4.36	−4.83	−0.83	−0.79	−0.01	0
(110)	−4.58	−4.87	−0.79	−0.83	−0.01	−0.01
(111)	−3.81	−4.42	−0.77	−0.76	−0.01	0

2.2 Synthesis and characterization of composition-segregated PdCo/CC catalyst

Based on the above results, multi-step pathways consisting of the oriented segregation and reconfigurations of a PdCo alloy were built on a substrate of a carbon cloth. A cyanogel (Fig. S1†) acting as the precursor was first coated on the carbon cloth (cyanogel/CC) and subsequently annealed at 450 °C in an Ar and NH_3 flow (60 mL min^{-1}) (for details, please see the Method section). The activation was performed in a 0.5 M H_2SO_4 solution by continuous EC cycling between −0.2 and +1.0 V (*vs.* SCE). The alloy generated by cyanogel ammonolysis (PdCo/CC) presented significant changes in morphology (Fig. 2). The scanning electron microscopy (SEM) images show that the uniform cyanogel film on CC (Fig. 2a) transforms to nanoparticles with a diameter of ~50 nm after NH_3 treatment (Fig. 2b). The round nanoparticles (Fig. 2b) were gradually transformed to a well-shaped dendritic nanostructure after EC treatment for 400 cycles (Fig. 2f; we denoted this product as $PdCo/CC_{400}$). As we expected, the EC cycling-induced structural evolution largely relied on the protector atmosphere. The product after annealing the cyanogel in an Ar atmosphere ($PdCo/CC_{Ar}$) retained the original structure after EC cycling (Table S4†). Numerous small holes were found on the surface of CC, which could be attributed to the oxidation etching from metal salts without NH_3 protection. When the precursor cyanogel was replaced by the mixture of metal salts (H_2PdCl_4–$Na_3Co(NO_2)_6$), the PdCo alloy could not be well mixed (here, denoted as Pd–Co/CC). Thus, after the same EC scanning cycles, the resulting catalyst (Pd–Co/CC_{400}) exhibited less morphology changes with respect to $PdCo/CC_{400}$. Furthermore, after using H_2PdCl_4 as the sole precursor, the as-formed Pd/CC_{400} also presented primary morphology. These results indicate that this structural evolution of the PdCo alloy may depend on the Co leaching process and Pd rearrangement, which is consistent with our expectation.

The X-ray powder diffraction (XRD) pattern of both PdCo/CC and $PdCo/CC_{Ar}$ shows five strong characteristic peaks of face-

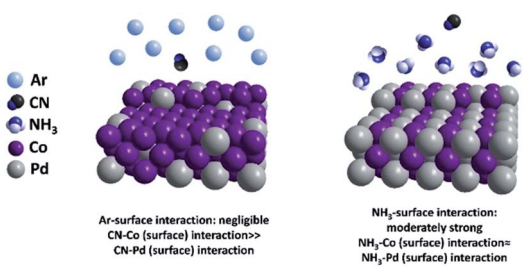

Fig. 1 Simulation results of surface interaction of Ar and NH_3 towards Co and Pd.

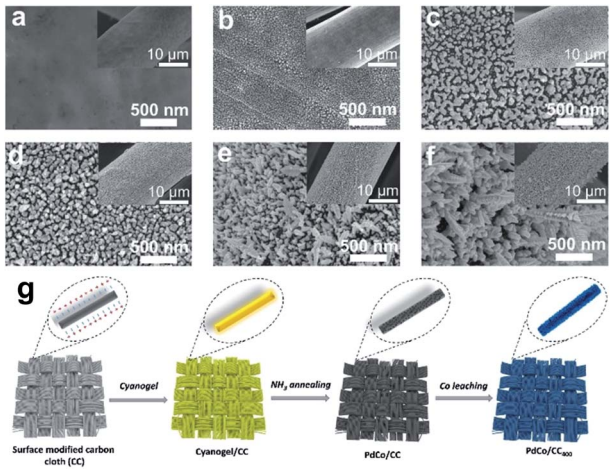

Fig. 2 Structural evolution from cyanogel/CC to PdCo/CC_{400}. With the increased number of EC scanning cycles, comparison of the PdCo/CC morphology at different cycles. SEM images of (a) cyanogel/CC, (b) PdCo/CC, (c) PdCo/CC_{50}, (d) PdCo/CC_{100}, (e) PdCo/CC_{200}, (f) PdCo/CC_{400}. (g) Schematic illustration of the conversion from cyanogel/CC to PdCo/CC_{400}.

centered cubic (fcc) crystals, namely, the (111), (200), (220), (311) and (222) planes (Fig. 3a). No significant characteristic peak of Co species was found from the XRD pattern for PdCo/CC, which could be attributed to the inclusion of Co in the Pd lattice and the formation of the PdCo alloy (PDF no. 00-050-1437).[29] Also, the intensity of the diffraction peaks in the XRD pattern exhibits a significant enhancement after EC cycling. Notably, the diffraction peaks of PdCo/CC_{400} shifted to lower 2θ values with respect to the corresponding peaks for PdCo/CC (Fig. 3b), suggesting that the product changed into a pure Pd phase (PDF no. 01-087-0638) due to successful dealloying.[30,31]

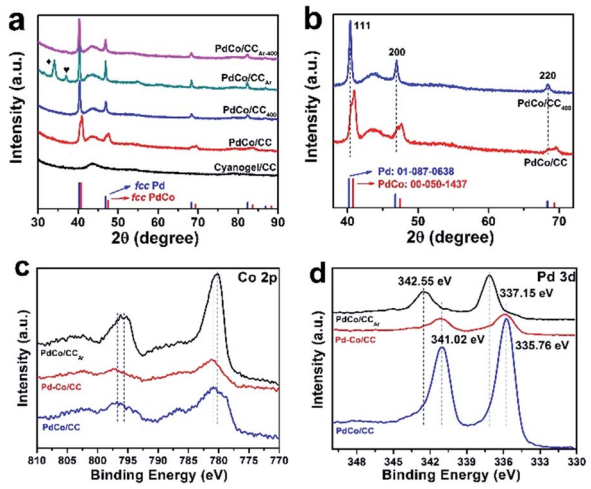

Fig. 3 Phase and interface characterizations of different samples. (a) XRD spectra of cyanogel/CC, PdCo/CC, and PdCo/CC_{Ar} before and after 400 EC cycles. The symbols denote the emerging cobalt oxides in PdCo/CC_{Ar}. (b) Enlarged view of XRD spectra of PdCo/CC and PdCo/CC_{400}. XPS core level spectra for (c) Co 2p and (d) Pd 3d of the PdCo/CC, PdCo/CC_{Ar} and Pd–Co/CC samples.

These results demonstrated that continuous EC cycling in the acid solution could result in the leaching of Co species from the PdCo alloy. It was found that PdCo/CC_{Ar} also displayed typical peaks of the fcc Pd phase but with a slight shift to a higher angle. The diffraction peaks located at 34.1° and 37.0° matched well with the strongest diffraction peaks of CoO (PDF no. 01-075-0419) and Co_3O_4 (PDF no. 01-074-1656), respectively. After EC cycling, the two peaks disappeared with the retention of other peaks, which can be ascribed to the dissolution of cobalt oxides on the PdCo/CC_{Ar} surface.

As presented in Fig. 3, X-ray photoelectron spectroscopy (XPS) analysis was conducted to explore the element distributions on the surface of the catalyst. Comparing the Co 2p (Fig. 3c) with Pd 3d (Fig. 3d) signals, it should be noted that the Co/Pd atomic ratio for the PdCo/CC_{Ar} sample is around 4. Without using a cyanogel as the alloy precursor, the resulting Co/Pd atomic ratio was ~2.9 for Pd–Co/CC. Even more noticeably, the Pd 3d intensity was very high for the NH_3-treated sample PdCo/CC, and the Co/Pd atomic ratio reached ~0.9, which was much lower than that of PdCo/CC_{Ar} and Pd–Co/CC. These results indicate that the Co concentration on the surface of PdCo/CC_{Ar} is very high (the effective analysis depth of XPS is limited to several nanometers underneath the surface) even to the point of phase segregation, which agreed with the results of XRD analysis. On the contrary, the ammonolysis of a cyanogel is inclined to form an alloy with more Pd atoms distributed near the surface of the nanostructure. Furthermore, it was also noted that the Pd 3d signals of PdCo/CC exhibited lower binding energies compared to those of PdCo/CC_{Ar}. These results suggested that because of the different elemental distributions on the surface, the acid leaching of Co atoms could result in much significant influences on the morphology of PdCo/CC. In this case, PdCo/CC has a surface with a balanced composition (slightly Pd-rich) with uniformly distributed Co atoms. With the dissolution of the Co species by EC cycling in an acid solution, all the neighboring Pd atoms on the surface became low-coordinated sites, which became unstable and loose. Subsequent Co leaching from the underneath alloy layer could further destroy the surface to expose more low-coordinated Pd atoms. For all the samples, all the near-surface Co species leached out after 400 EC cycles (Fig. S2†). In addition, the peaks of the Pd 3d signals shifted to lower binding energies (Fig. S2†), which was ascribed to the successful dealloying process by dissolving the Co species.[32] The whole process induced more preferred orientations and active sites in the new nanostructure.

2.3 The effect of acid leaching Co on PdCo/CC

XPS was further performed on PdCo/CC of different EC cycles to investigate the evolution of their composition by the leaching process of the Co species. As shown in Fig. 4b, the new peaks of PdCo/CC appearing for the Co 2p XPS signals can be attributed to Co^0 (at ~779.6 and 794.6 eV) of the PdCo alloy.[33,34] The peaks at the binding energies of ~781.9 eV and 797.2 eV with two shake-up satellites were assigned to Co^{x+} (cobalt oxides/cobalt nitride).[35,36] The formation of Pd^0 was demonstrated by the

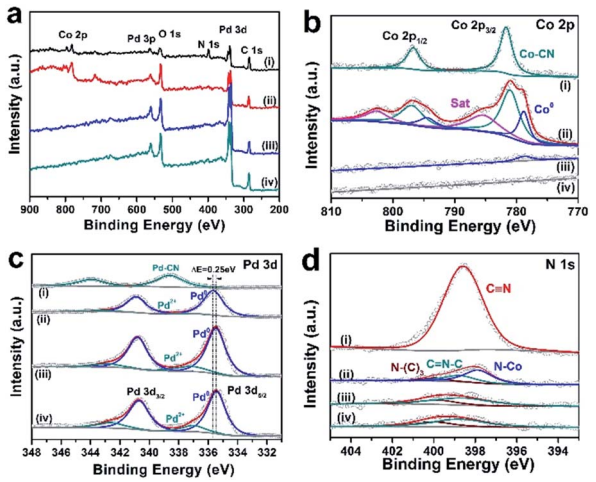

Fig. 4 Evolution of element composition on the surface of the samples. (a) XPS full spectra for cyanogel/CC (curve i), PdCo/CC (curve ii), PdCo/CC_{200} (curve iii), and PdCo/CC_{400} (curve iv), and their core level spectra for (b) Co 2p, (c) Pd 3d and (d) N 1s.

obvious shoulder peak at ~335.8 eV (Fig. 4c).[37,38] For the N 1s signals (Fig. 4d), the C═N peak of the cyanogel at ~399.0 diminished with the appearance of a new weak peak ascribed to Co_4N at ~397.9 eV.[39] These results demonstrated that the noble-metal and the transition-metal centers in the cyanogel were reduced to lower oxidation states after the annealing treatment in NH_3 at a high temperature. The surface Co atoms are more susceptible to oxidation than the Pd atoms and thus, the majority of the surface Co atoms were oxidized and the surface Pd atoms were mainly in the metallic state.[8] As shown in Fig. 4b, when continuous EC cycling was carried out for 200 cycles (PdCo/CC_{200}), the Co 2p signals decreased considerably and ultimately disappeared at the 400th cycle (PdCo/CC_{400}). At the same time, as shown in Fig. 4d, the N 1s peak at ~397.8 eV, which is ascribed to Co–N, is hard to be observed at the 200th cycle, and it completely disappears at the 400th cycle, indicating the removal of Co_4N by potential cycling. However, the N 1s peaks at 398.8 eV (attributed to C═N–C) and 399.8 eV (attributed to N–$(C)_3$) from the N-doped CC do not exhibit any obvious change. On the other hand, the Pd 3d peaks increase after EC cycling and present a shift (*ca.* 0.25 eV) to lower binding energy. This shift can be ascribed to the disappearance of the strong electron interactions involving Pd and Co in the PdCo alloy.[32]

The influence of EC cycling on the surface of the catalyst was further investigated with transmission electron microscopy (TEM) (Fig. S3†). Electron diffraction patterns were recorded on the nanocrystals to align them along the <110> axis, which showed a single-crystal structure for both PdCo/CC and PdCo/CC_{400} in the selected area. Fig. S3a and c† show that EC cycling transforms the morphology of the PdCo alloy from nanoparticles to a dendritic nanostructure, which is consistent with the SEM analysis. The high-resolution TEM (HR-TEM) images verify that the cyanogel is converted to the PdCo alloy owing to the reduction property of cyanide ligands and NH_3 at a high temperature.[29,40] The interplanar distances of 1.9 and 2.2 Å corresponding to the (200) and (111) lattice plane spacings in the fcc PdCo alloy slightly increased after EC cycling (Fig. S3b and d†), which wasattributed to the effect of the decreased amounts of Co in the PdCo alloy. This was also consistent with the XRD results, indicating the successful dealloying process. The aberration-corrected TEM images (Fig. 5) reveal the dendritic morphology of PdCo/CC_{400} more clearly. This well-shaped dendritic nanostructure was composed of overlapped ultrathin nanosheets (Fig. S4†). A number of high-index {*hkk*} facets such as the {200}, {311}, and {211} surfaces that have a large density of atomic steps and dangling bonds were captured in the aberration-corrected HR-TEM image of PdCo/CC_{400} (Fig. 5d, e and S5d†). For PdCo/CC, a series of the {*hhl*} facets was frequently observed around the surface, resulting in an overall profile close to that of the round nanoparticles (Fig. S5†). The variation of the atomic arrangement on the surface facets of the PdCo alloy after EC cycling contributed to the evolution of the nanostructures. These atomic steps consisted of the (111) terraces separated by the (110) or (200) steps; their corresponding atomic models are shown in Fig. S6.† Note that the dominant {*hkk*} surfaces after EC cycling have more low-coordinated atomic steps than the {*hhl*} surfaces before EC cycling, which agrees with our expectation that the etching of Co from the surface having a balanced composition can generate more low-coordinated sites. For example, {311} has 31% more step sites than {331}, while {211} has 22% more step sites than {221} (Table S5†). Thus, the higher density of the low-coordinated sites favored H adsorption on the surface, which could be beneficial for HER. The EDX elemental mappings obtained by HAADF-STEM proved that the Pd and Co elements were distributed homogeneously throughout the whole area for PdCo/CC (Fig. S7†). After EC cycling, Pd was still distributed across the dendrite, but Co was located only in the center

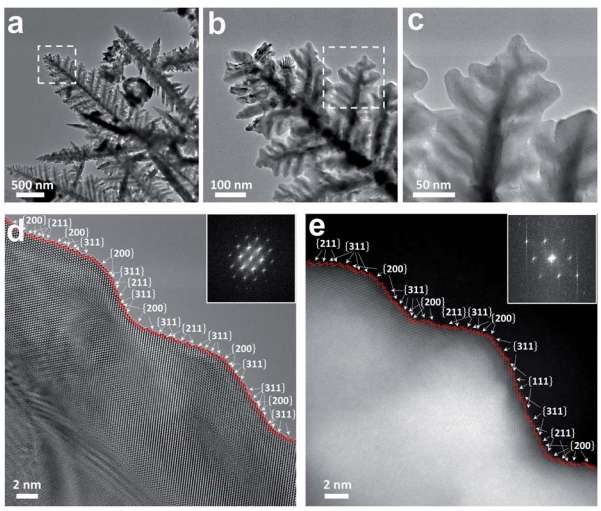

Fig. 5 Morphology characterization of PdCo/CC_{400}. (a–c) Aberration-corrected TEM images of PdCo/CC_{400} and the enlarged area is marked with a white dashed box. Aberration-corrected (d) HR-TEM and (e) HAADF-STEM images of PdCo/CC_{400} viewed along the <110> direction showing their surface atomic steps made of different facets. Inset is the corresponding FFT pattern.

region, demonstrating that Co on the outer part of the nanocrystals was etched away (Fig. S8†); this was further confirmed by line scan analysis (Fig. S9†).

2.4 HER performance of pristine PdCo/CC and PdCo/CC_{400}

The HER catalytic activity of the as-prepared PdCo/CC was evaluated using a three-electrode system in a 0.5 M aqueous H_2SO_4 solution. To achieve the optimized catalytic property, a series of synthesis conditions were investigated, including the cyanogel concentration (Fig. S10†), cyanogel loading amount (Fig. S11†), surface charges of the carbon cloth (Fig. S12†), annealing temperature (Fig. S13†), and time duration (Fig. S14†). The optimized conditions of the positively charged CC coated with the cyanogel (25 mM) for three times followed by annealing in an NH_3 atmosphere at 450 °C for 1 h were applied in the subsequent study to prepare the PdCo/CC catalyst. As shown in Fig. 6a, the as-formed PdCo/CC affords current density of 100 mA cm^{-2} at an overpotential of −92.3 mV. EC cycling induced Co leaching, which resulted in gradual improvements in the HER catalysis performance with the cycling numbers.

PdCo/CC_{400} afforded intensively boosted HER activity with a current density of 100 mA cm^{-2} only at an overpotential of 75.0 mV. It should be noted that the catalyst did not exhibit further changes in the catalytic activity (Fig. 6d) and morphology (Table S4†) after 400 EC cycles. The cathodic peak around 0.02 V was assigned to the overpotential deposition (OPD) of hydrogen adsorption on the alloy.[41,42] To evaluate the EC-induced acid leaching on the electrochemical characteristics of the resultant catalyst, we measured the HER catalytic performances of the PdCo/CC_{Ar}, Pd–Co/CC and Pd/CC electrodes in 0.5 M H_2SO_4 before and after EC cycling in comparison to that of Pt/C (measured in this work by loading 20% commercial Pt/C on to CC at the same mass density as PdCo) (Fig. S15–S17†). The EC cycling treatment resulted in a poor boosting effect for the HER activity (Fig. 6b) and fewer changes in morphology (Table S4†) compared to that for PdCo/CC_{400} prepared in NH_3. These results indicated that both ammonolysis and cyanogel played a great role in achieving high HER activity and the boosting of activity largely depended on the element ratio and distribution on the surface of the PdCo alloy, which decided the Co leaching process and Pd rearrangement. PdCo/CC_{400} showed an impressively low Tafel slope of 22.6 mV dec^{-1}, which was smaller than those of PdCo/CC (53.2 mV dec^{-1}), Pt/C (31.7 mV dec^{-1} measured in this work), Pt plate (37.2 mV dec^{-1} measured in this work), and other representative Pd-based HER electrocatalysts (Fig. 6c and Table S6†). Generally, a Tafel slope close to 30 mV dec^{-1} suggests that the mechanism governing the HER reaction over our catalysts is the Volmer–Tafel (electrochemical hydrogen adsorption-recombination step) mechanism, where the latter is the rate-determining step, as shown in the Experimental section of ESI.†[43] In terms of current density normalized by geometric area, there is a difference in the different batches of syntheses and measurements such as the deviation of the LSV curves of PdCo/CC_{400} (Fig. 6a, b and d) although the trend of enhancement by EC cycling is the same. To compare the intrinsic activities of the catalyst, their turnover frequency (TOF) values corresponding to the number of hydrogen molecules evolved per second per active site were calculated by electrochemically active surface area (ECSA) and mass loading, respectively (Fig. S18 and S19†). Compared with other palladium-based catalysts, PdCo/CC_{400} showed the highest TOF values of 6.48 s^{-1} and 10.96 s^{-1} at the overpotentials of $\eta = 70$ mV and $\eta = 75$ mV, respectively, indicating excellent intrinsic HER activity (Table S7†). The stability of PdCo/CC_{400} was assessed by applying 1000 potential scanning cycles between −0.2 and 1.0 V. As shown in Fig. 6d, the HER catalytic current almost overlays with the initial one, indicating the excellent HER catalytic durability of PdCo/CC_{400} in an acid electrolyte. Furthermore, PdCo/CC_{400} also exhibited outstanding long-term operation stability to maintain the high HER current density of ~60 mA cm^{-2} beyond 48 h. This good stability could be attributed to the hierarchical structure formed by the open nanostructured morphologies deposited directly on a conductive support (carbon cloth), which benefited the evolution of hydrogen bubbles from the large electrode surface and prevented the nanosheets from re-stacking.[44,45] This exceptional durability offers PdCo/CC_{400} promising potentials in practical applications over a long term.

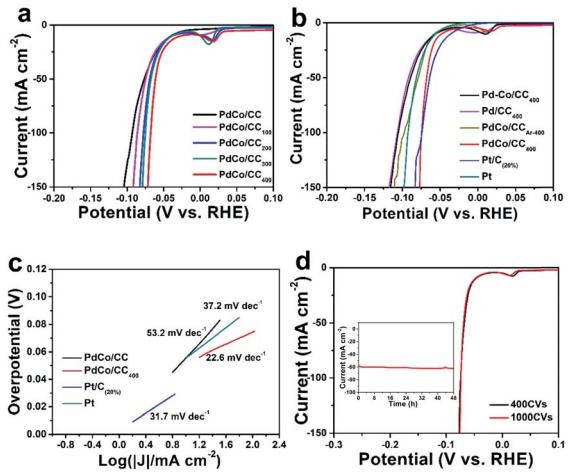

Fig. 6 Electrocatalytic activities of different PdCo alloys in 0.5 M H_2SO_4 solutions. (a) HER polarization curves of PdCo/CC before and after different EC cycles. (b) HER polarization curves of various catalysts. (c) Tafel plots recorded on the PdCo/CC, PdCo/CC_{400}, 20% Pt/C and Pt. (d) Stability tests of PdCo/CC_{400} catalyst through potential cycling, in which the polarization curves before and after 1000 potential cycles are displayed. Inset: time dependence of cathodic current density during electrolysis over 48 h at a fixed overpotential of −75 mV, respectively.

3. Conclusions

In conclusion, we designed and verified a novel and effective strategy to prepare a PdCo alloy bound by abundant high-index facets. Our DFT calculations and experimental data demonstrated that the elemental distribution in the alloys is determined by the protector atmosphere and alloy precursor. We

used this property to tune the surface composition of the alloy and then etch the impurities under EC cycling to generate high density of active sites. The synthesized catalyst exhibited extraordinary activity and stability toward the HER reaction. This work thus provides a promising and cost-effective method to develop a highly efficient noble-metal catalyst for water splitting reactions and other industrially important applications.

4. Experimental section

4.1 Computational methodology

In this work, three low-index surfaces ((100), (110) and (111)) of pure fcc-Co and pure Pd were considered. The periodic 2-D slab models with 5 atoms layers and the bottom 2 layers were fixed; others were relaxed. Along the *Z* axis, there was a 15 Å vacuum space on every surface. For (100) and (111) of Co and Pd, (4×4) unit cells are used, and (110) is a (3×4) unit cell. All the slabs were modeled by a $(3 \times 3 \times 1)$ of *K*-points. The adsorption energies of CN, NH_3 and Ar on the pure Pd surface and the pure Co surface were calculated by Vienna *Ab Initio* Simulation Package (VASP) to perform spin-polarized density functional theory (DFT) calculations.[46] The Perdew, Burke and Erzernhof (PBE) functional was employed.[47] The cutoff of the plane-wave expansion was 400 eV. The convergence for the electronic self-consistent was set to 10^{-5} eV, and the force convergence criterion in a conjugate-gradient algorithm was 0.02 eV $Å^{-1}$.

4.2 Preparation of CC-PEI

The CC substrate was cut into the appropriate size (1 cm × 1 cm) and cleaned with acetone, ethanol, and distilled water; then, it was treated by ultrasonication with a mixed solution of concentrated HNO_3 and H_2SO_4 (v/v = 1 : 3) and dried in an oven at 60 °C for 2 h. CC-PEI was prepared by immersing negatively charged CC into positively charged PEI (1 wt% solution in water), and the mixture underwent heat treatment in an oven at 60 °C for 5 h. Excess PEI was removed by deionized (DI) water washing.

4.3 Preparation of PdCo/CC

In a typical synthesis, 80 μL of 25 mM H_2PdCl_4 and 40 μL of 25 mM $K_3Co(CN)_6$ solutions were mixed to form a cyanogel; then, CC-PEI was incubated in it for 24 h and dried in air. After this procedure was repeated three times, the resulting cyanogel/CC was carefully washed with DI water and then dried in air. Alloys were produced from the cyanogel by heating the cyanogel/CC samples in a furnace at 450 °C for 1 h with a 10 °C min ramp under flowing NH_3 or Ar (60 mL min^{-1}). The preparation protocol of Pd/CC and Pd–Co/CC was similar to that of PdCo/CC except that the precursor was replaced by the mixture of metal salts (H_2PdCl_4 and $Na_3Co(NO_2)_6$) or H_2PdCl_4 was used as the sole precursor.

4.4 Characterization

The morphologies of the nanoparticles were characterized by field-emission scanning electron microscopy (FESEM; Hitachi S-4800, Tokyo, Japan). Transmission electron microscopy (TEM) and high-angle annular dark-field scanning transmission electron microscopy (HAADF-STEM) were conducted on FEI Titan G2 60–300. Part of the TEM analysis was carried out on JEOL 2000. X-ray diffraction (XRD) patterns were acquired on an X'Pert X-ray diffraction spectrometer (Philips, Guildford, Surrey, U.K.) with a Cu Kα X-ray source (Wellesley, MA). X-ray photoelectron spectroscopy (XPS) was performed on a PerkinElmer Physical Electronics 5600 spectrometer using Al Kα radiation at 13 kV as the excitation source.

4.5 Electrochemical tests

Electrochemical measurements were carried out on a CHI660E electrochemical workstation (CH Instrument Co. Shanghai) with a typical three-electrode system. The binder-free PdCo/CC was directly used as the working electrode. Electrochemically inert polyimide tape was employed to define the 1 cm^2 electrode area. A Pt sheet and a saturated calomel electrode (SCE) were used as the counter and reference electrodes, respectively. Electrochemically (EC) cycling was operated in N_2-saturated 0.5 M H_2SO_4 by cyclic voltammetry (CV) from −0.2 to 1.0 V *vs.* SCE at a scan rate of 200 mV s^{-1}. The electrochemical active surface area (ECSA) of the as-prepared catalyst was calculated by CV, which was carried out in the same condition except for a slower scan rate (50 mV s^{-1}). The polarization curves before and after cycling were recorded under quasi-equilibrium conditions at a scan rate of 5 mV s^{-1} in N_2-saturated 0.5 M H_2SO_4 to measure the HER performance. All potentials were referenced to a reversible hydrogen electrode (RHE) by adding a value of E_{SCE} +0.242 V. All polarization curves were corrected for *iR* losses.

Conflicts of interest

There are no conflicts of interest to declare.

Acknowledgements

This research is supported by the National Natural Science Foundation of China (No. 21775016, 21874013, 11574340, 21773287), Fundamental Research Funds for the Central Universities (N182410008-1, N170502003, N170506005, N170908001) and the Talent Project of Revitalizing Liaoning (XLYC1807165).

References

1 Z. W. Seh, J. Kibsgaard, C. F. Dickens, I. Chorkendorff, J. K. Nørskov and T. F. Jaramillo, *Science*, 2017, **355**, 146.
2 M. Luo and S. Guo, *Nat. Rev. Mater.*, 2017, **2**, 17059.
3 J.-Y. Zhang, T. He, M. Wang, R. Qi, Y. Yan, Z. Dong, H. Liu, H. Wang and B. Y. Xia, *Nano Energy*, 2019, **60**, 894–902.
4 L. Bu, N. Zhang, S. Guo, X. Zhang, J. Li, J. Yao, T. Wu, G. Lu, J.-Y. Ma, D. Su and X. Huang, *Science*, 2016, **354**, 1410–1414.
5 X. Huang, Z. Zhao, L. Cao, Y. Chen, E. Zhu, Z. Lin, M. Li, A. Yan, A. Zettl, Y. M. Wang, X. Duan, T. Mueller and Y. Huang, *Science*, 2015, **348**, 1230–1234.

6 L. Zhang, L. T. Roling, X. Wang, M. Vara, M. Chi, J. Liu, S.-I. Choi, J. Park, J. A. Herron, Z. Xie, M. Mavrikakis and Y. Xia, *Science*, 2015, **349**, 412–416.
7 J. D. Benck, T. R. Hellstern, J. Kibsgaard, P. Chakthranont and T. F. Jaramillo, *ACS Catal.*, 2014, **4**, 3957–3971.
8 C. Chen, Y. Kang, Z. Huo, Z. Zhu, W. Huang, H. L. Xin, J. D. Snyder, D. Li, J. A. Herron, M. Mavrikakis, M. Chi, K. L. More, Y. Li, N. M. Markovic, G. A. Somorjai, P. Yang and V. R. Stamenkovic, *Science*, 2014, **343**, 1339–1343.
9 M. Li, Z. Zhao, T. Cheng, A. Fortunelli, C.-Y. Chen, R. Yu, Q. Zhang, L. Gu, B. V. Merinov, Z. Lin, E. Zhu, T. Yu, Q. Jia, J. Guo, L. Zhang, W. A. Goddard, Y. Huang and X. Duan, *Science*, 2016, **354**, 1414–1419.
10 Y.-Q. Kang, Q. Xue, Y. Zhao, X.-F. Li, P.-J. Jin and Y. Chen, *Small*, 2018, **14**, 1801239.
11 G. A. Somorjai and D. W. Blakely, *Nature*, 1975, **258**, 580.
12 F. Wang, C. Li, L.-D. Sun, H. Wu, T. Ming, J. Wang, J. C. Yu and C.-H. Yan, *J. Am. Chem. Soc.*, 2011, **133**, 1106–1111.
13 Y. Yu, Q. Zhang, B. Liu and J. Y. Lee, *J. Am. Chem. Soc.*, 2010, **132**, 18258–18265.
14 N. Tian, Z.-Y. Zhou, S.-G. Sun, Y. Ding and Z. L. Wang, *Science*, 2007, **316**, 732–735.
15 Z.-L. Wang, X.-F. Hao, Z. Jiang, X.-P. Sun, D. Xu, J. Wang, H.-X. Zhong, F.-L. Meng and X.-B. Zhang, *J. Am. Chem. Soc.*, 2015, **137**, 15070–15073.
16 Y. Yan, T. He, B. Zhao, K. Qi, H. Liu and B. Y. Xia, *J. Mater. Chem. A*, 2018, **6**, 15905–15926.
17 L. Su, X. Cui, T. He, L. Zeng, H. Tian, Y. Song, K. Qi and B. Y. Xia, *Chem. Sci.*, 2019, **10**, 2019–2024.
18 C. G. Morales-Guio, L.-A. Stern and X. Hu, *Chem. Soc. Rev.*, 2014, **43**, 6555–6569.
19 J.-Y. Zhang, H. Wang, Y. Tian, Y. Yan, Q. Xue, T. He, H. Liu, C. Wang, Y. Chen and B. Y. Xia, *Angew. Chem., Int. Ed.*, 2018, **57**, 7649–7653.
20 L. S. R. Silva, C. V. S. Almeida, C. T. Meneses, E. A. Batista, S. F. Santos, K. I. B. Eguiluz and G. R. Salazar-Banda, *Appl. Catal., B*, 2019, **251**, 313–325.
21 G. Valenti, A. Boni, M. Melchionna, M. Cargnello, L. Nasi, G. Bertoni, R. J. Gorte, M. Marcaccio, S. Rapino, M. Bonchio, P. Fornasiero, M. Prato and F. Paolucci, *Nat. Commun.*, 2016, **7**, 13549.
22 S. Rej, C.-F. Hsia, T.-Y. Chen, F.-C. Lin, J.-S. Huang and M. H. Huang, *Angew. Chem., Int. Ed.*, 2016, **55**, 7222–7226.
23 F.-M. Li, Y.-Q. Kang, R.-L. Peng, S.-N. Li, B.-Y. Xia, Z.-H. Liu and Y. Chen, *J. Mater. Chem. A*, 2016, **4**, 12020–12024.
24 J. Li, P. Zhou, F. Li, R. Ren, Y. Liu, J. Niu, J. Ma, X. Zhang, M. Tian, J. Jin and J. Ma, *J. Mater. Chem. A*, 2015, **3**, 11261–11268.
25 H.-L. Jiang and Q. Xu, *J. Mater. Chem.*, 2011, **21**, 13705–13725.
26 M. Vondrova, C. M. Burgess and A. B. Bocarsly, *Chem. Mater.*, 2007, **19**, 2203–2212.
27 Y. Zhao, J. Bai, X.-R. Wu, P. Chen, P.-J. Jin, H.-C. Yao and Y. Chen, *J. Mater. Chem. A*, 2019, **7**, 16437–16446.
28 V. G. Ruiz, W. Liu and A. Tkatchenko, *Phys. Rev. B*, 2016, **93**, 035118.
29 M. Vondrova, T. Klimczuk, V. L. Miller, B. W. Kirby, N. Yao, R. J. Cava and A. B. Bocarsly, *Chem. Mater.*, 2005, **17**, 6216–6218.
30 W. Wang, D. Zheng, C. Du, Z. Zou, X. Zhang, B. Xia, H. Yang and D. L. Akins, *J. Power Sources*, 2007, **167**, 243–249.
31 T. Gunji, R. H. Wakabayashi, S. H. Noh, B. Han, F. Matsumoto, F. J. DiSalvo and H. D. Abruña, *Electrochim. Acta*, 2018, **283**, 1045–1052.
32 A.-L. Wang, X.-J. He, X.-F. Lu, H. Xu, Y.-X. Tong and G.-R. Li, *Angew. Chem., Int. Ed.*, 2015, **54**, 3669–3673.
33 Y. Li, P. Zhou, Z. Dai, Z. Hu, P. Sun and J. Bao, *New J. Chem.*, 2006, **30**, 832–837.
34 S. Choi and M. Oh, *Angew. Chem., Int. Ed.*, 2019, **58**, 866.
35 T. Varga, G. Ballai, L. Vásárhelyi, H. Haspel, Á. Kukovecz and Z. Kónya, *Appl. Catal., B*, 2018, **237**, 826–834.
36 M. C. Biesinger, B. P. Payne, A. P. Grosvenor, L. W. M. Lau, A. R. Gerson and R. S. C. Smart, *Appl. Surf. Sci.*, 2011, **257**, 2717–2730.
37 H. Xue, J. Tang, H. Gong, H. Guo, X. Fan, T. Wang, J. He and Y. Yamauchi, *ACS Appl. Mater. Interfaces*, 2016, **8**, 20766–20771.
38 Z. Zhang, S. Liu, X. Tian, J. Wang, P. Xu, F. Xiao and S. Wang, *J. Mater. Chem. A*, 2017, **5**, 10876–10884.
39 Y. Zhang, B. Ouyang, J. Xu, G. Jia, S. Chen, R. S. Rawat and H. J. Fan, *Angew. Chem., Int. Ed.*, 2016, **55**, 8670–8674.
40 M. Vondrova, P. W. Majsztrik, S. Gould and A. B. Bocarsly, *Chem. Mater.*, 2005, **17**, 4755–4757.
41 T. Bhowmik, M. K. Kundu and S. Barman, *ACS Catal.*, 2016, **6**, 1929–1941.
42 S. Bai, C. Wang, M. Deng, M. Gong, Y. Bai, J. Jiang and Y. Xiong, *Angew. Chem., Int. Ed.*, 2014, **53**, 12120–12124.
43 Y. Li, H. Wang, L. Xie, Y. Liang, G. Hong and H. Dai, *J. Am. Chem. Soc.*, 2011, **133**, 7296–7299.
44 Y. Zhao, S. Xing, X. Meng, J. Zeng, S. Yin, X. Li and Y. Chen, *Nanoscale*, 2019, **11**, 9319–9326.
45 A. Sivanantham and S. Shanmugam, *Appl. Catal., B*, 2017, **203**, 485–493.
46 G. Kresse and J. Hafner, *Phys. Rev. B: Condens. Matter Mater. Phys.*, 1993, **47**, 558.
47 J. P. Perdew, J. A. Chevary, S. H. Vosko, K. A. Jackson, M. R. Pederson, D. J. Singh and C. Fiolhais, *Phys. Rev. B: Condens. Matter Mater. Phys.*, 1992, **46**, 6671–6687.

